Dynamic Response and Stability Analysis of High-Speed Railway Subgrade in Karst Areas

LI XIN[ID], BAI MINGZHOU, WEI ZIJUN, LI PENGXIANG, SHI HAI, AND ZHANG YE

School of Civil Engineering, Beijing Jiaotong University, Beijing 100044, China

Corresponding author: Bai Mingzhou (541515520@qq.com)

ABSTRACT The increase in railway coverage significantly increased the railway mileage in karst areas. However, the fragile ecosystem in karst areas and weak mechanical performance in cavities cause hidden railway safety hazards. Even with the crucial stability and safety of railways in karst areas, there is only limited research conducted on the dynamic response of railway subgrade and the influence of hidden soil holes on the stability under different conditions. In this study, the Guizhou section of the Shanghai–Kunming high-speed railway was chosen as the research area. On-site monitoring and simulations using ABAQUS were performed to study the dynamic response of the subgrade under the dynamic load of a train. The influence of the soil hole, axle load, and vehicle speed on the dynamic response law and stability of the subgrade were considered based on the model rationality verification. Previous studies have demonstrated the considerable impact of soil holes on the dynamic response characteristics and stability of roadbeds. The ambient vibration frequency of the train was concentrated at 10–60 Hz. Under train load, the amplitude of the dynamic response parameters of each subgrade structural layer increased with the axle load; however, the increase in speed exhibited a greater impact on the vertical dynamic displacement and dynamic stress than on the dynamic acceleration, which affected the stability of the soil hole and roadbed. This study summarized the dynamic response characteristics of subgrade in karst areas under different conditions, thereby providing a design reference for high-speed railways in karst areas.

INDEX TERMS Dynamic response, high-speed railway, karst, subgrade, vibration monitoring.

I. INTRODUCTION

China's karst area accounts for approximately 37.8% of its total land area, and the national railway operating mileage is more than 139 000 km, accounting for two-thirds of the world's high-speed railway operating mileage. In existing high-speed railways, the length of the section located in areas with high-risk karst collapse is greater than 2000 km. Owing to karst collapse, train operations are often interrupted for thousands of hours, which seriously endangers the operation and safety of the railway [1], [2].

Railway engineering is affected by karst collapse throughout the construction and operation cycles. Train vibration, karst cavities, and other factors, the mechanical properties and deformation characteristics of rock and soil around railways environment affects the stability of the railway subgrade and induces subgrade instability. Therefore, it is of great practical significance to study the influence of hidden

soil holes on the stability of railway subgrade in karst areas [3], [4].

This study considered the Guizhou section of the Shanghai–Kunming high-speed railway, and investigated the influence of karst collapse and train vibration load on subgrade stability and dynamic response by combining field tests and numerical simulations. The main contributions of this study are as follows:

1) By performing field monitoring of the vibration acceleration of the subgrade under driving conditions, the vibration response law of the ground around the subgrade was obtained by analyzing the data in the time and frequency domains.

2) To address the vibration problem of high-speed railways under operational conditions, a three-dimensional finite element numerical simulation model of the dynamic coupling of high-speed train–ballastless track–subgrade structure in karst areas was established. The development of the model, selection of structural elements, and realization of the boundary conditions are discussed.

The associate editor coordinating the review of this manuscript and approving it for publication was Jesus Felez[ID].

3) The monitoring results were used to verify the accuracy of the mathematical model. The differences in the dynamic displacement, acceleration, and dynamic stress of the subgrade and foundation with and without underlying soil holes, and distribution characteristics and propagation rules in the subgrade were analyzed in the time domain.

4) Using a quantitative analysis method, the dynamic response law of the train vibration load along the subgrade depth direction, and its influence on the subgrade stability under different train axle loads and running speeds were studied. This provides a reference for the durability and safety design of high-speed railway subgrades in karst areas.

The remainder of this paper is organized as follows. Section II presents a review of existing relevant literature. Section III presents the methodology used in the present study, which utilizes relevant research on the dynamic response of railway subgrades in karst areas and combines on-site train vibration frequency acquisition and numerical simulation methods. The results are discussed in Section IV. Considering the presence or absence of soil holes, and different train axle loads and vehicle speeds, the vertical dynamic stress, dynamic strain, and dynamic acceleration of different high-speed railway subgrade layers are comprehensively studied and compared. Finally, Section V concludes the paper.

II. LITERATURE REVIEW

Large-scale karst ground collapse disasters have occurred in more than 16 countries including China, the United States, and Spain. Thus, the operational safety of high-speed railways passing through development areas containing karsts is crucial. Regarding the dynamic response and stability of high-speed railway subgrades in karst areas, in-depth research has been conducted focusing on three aspects: karst collapse theory, influence of karst soil holes on subgrade stability, and dynamic response of hidden soil hole subgrade under train vibration load.

A. KARST COLLAPSE THEORY

Previous researchers have studied the formation mechanism of karst collapse through field investigation, and verified its accuracy through long-term monitoring and targeted treatment. The relevant results noted that the collapse mechanism of karst areas caused by rainfall, mining, groundwater discharge, and other factors is mainly attributed to erosion due to the decline of the groundwater level. In addition, the sharp decline of groundwater level and buoyancy forms a hydraulic gradient, which accelerates the seepage velocity of groundwater and induces collapse [5]–[7]. Although the natural reduction of groundwater causes karst collapse, several scholars believe that the main reason for karst collapse is the artificial extraction of groundwater, which causes local high negative pressure areas that loosens rocks and soil particles. This concept led to the development of the vacuum suction theory [8], [9]. Karst collapse is caused by the water–soil–rock interaction. In addition to water and aerodynamic

factors, human activities, such as train vibrations, are among the main causes of karst collapse. With the development of various testing and analysis methods, the mechanism of karst collapse induced by natural phenomena and human engineering activities have been investigated through model tests, chemical analyses, and mathematical models. Thus, karst collapse theories, such as dissolution and disintegration, CO vibration theory, vibration liquefaction, and seepage pressure effect, have been proposed. The relevant systems have also been improved [10], [11].

B. STABILITY ANALYSIS OF THE HIGH-SPEED RAILWAY SUBGRADE IN KARST AREA

The stability analysis of the railway subgrade in a karst area is important in ensuring safe railway operation. At present, the research on the stability of railway subgrade in karst areas mainly focuses on the formation mechanism, prediction of karst collapse, and stability evaluation of the underlying soil hole in the subgrade. There are three main methods for the stability analysis of karst subgrade: qualitative analysis methods, which provide non-quantitative conclusions for karst development and subgrade conditions according to the geological conditions [12]; semi-quantitative analysis methods, which combine approximate calculation and empirical analysis based on the semi-quantitative structural mechanics theory [13]; and quantitative analysis methods, which combine geological data and physical parameters, selects the main control factors, and simplifies the complex working conditions to the ideal model for analysis and calculation [14]. There have been several studies on the stability and critical failure conditions of subgrade in karst areas with different tunnel types, buried depth, subgrade size, and other characteristics through indoor model tests, mathematical and statistical derivations, intelligent algorithms, and various finite element simulation methods; thus, several targeted non-quantitative, semi-quantitative, and quantitative conclusions have been developed. These studies have considerable significance for the subgrade stability analysis under similar conditions [15]–[17].

C. DYNAMIC RESPONSE OF SUBGRADE SOIL

With the continuous improvement of train running speed and traction quality, there is an increasing importance for the stability evaluation of high-speed railway subgrade in terms of various factors, such as wheel–rail dynamic principle, subgrade environment, and mechanical properties of subgrade soil [18]. One of the basic methods of determining the train vibration load is empirical fitting through the combination of theoretical and test data.

The research on the dynamic response of subgrade under complex environmental factors has also gone through various stages. The research on this topic has shifted from field monitoring and data analysis to simplified indoor tests and theoretical derivations using field data, and then to numerical simulation under the condition of simplifying the environment and highlighting key factors [19]–[21].

The dynamic stress response of railway subgrade was first studied in European and American countries. These studies focused on the treatment of environmental noise and vibration effect, analysis of the acceleration and velocity time history characteristics of the subgrade under different vehicle types, and frequency spectrum analysis through Fourier transform (FTT) [22], [23]. Based on these reports, other scholars have analyzed the dynamic response of railway subgrade vibration. According to the characteristics of different railway sections, vehicle types, wheel–rail, subgrade, and environment, nonlinear models of the track–subgrade coupling have been established through numerical simulation. In-depth analyses have been conducted on the dynamic response of subgrade soil under train vibration with different vibration accelerations and distribution characteristics [24]–[27].

Thus, various karst collapse mechanisms have been developed throughout years of research with a focus on the railway subgrade in karst sections using quantitative, semi-quantitative, and qualitative methods. Most of the existing evaluation methods of the dynamic stress response of subgrade under train load are applied to a specific environment for targeted analysis and research. In most studies, there is less emphasis on combining the stability analysis of the subgrade in karst sections with the dynamic stress analysis of the subgrade under train load. In this study, considering the train load, and interaction between the subgrade and karst soil hole, the stability of high-speed railway subgrade is analyzed through numerical simulations. Moreover, the dynamic stress response characteristics of the subgrade in these areas under train vibrations are studied.

III. METHODOLOGY

A. DEVELOPMENT OF THE DYNAMIC RESPONSE MODEL BASED ON TRAIN–TRACK–SUBGRADE COUPLING

The settlement deformation and dynamic stability of the subgrade are important factors that affect the smoothness and durability of the ballastless track of high-speed railways. Using the ABAQUS/explicit module, and considering the subgrade structure and karst characteristics of the Guizhou section of the Shanghai–Kunming high-speed railway, this study established an integrated dynamic coupling model considering the train track road bedrock soil environment.

1) MODELING PROCESS

The model is a vibration-coupled system that includes spatial, time-varying, and nonlinear solutions. The vehicle and track subgrade were regarded as two subsystems. The coupling was realized through contact elements. The relationship between the mass, damping, stiffness, and vector matrix of the load was established. After the discretization of the structure, the train–track–subgrade coupling vibration equation can be expressed as (1):

$$[M]\{\ddot{X}\}(t+\Delta t) + [C]\{\dot{X}\}(t+\Delta t) + [K]\{X\}(t+\Delta t)$$
$$= \{P\}(t+\Delta t), \quad (1)$$

where [M] is the mass matrix of the high-speed train-ballastless track-subgrade system, [C] is the damping matrix of the high-speed train–ballastless track–subgrade system, [K] is the stiffness matrix of the high-speed train–ballastless track–subgrade system, $\{\ddot{X}\}$ is the generalized acceleration vector of the coupled system, $\{\dot{X}\}$ is the generalized velocity vector of the coupled system, $\{X\}$ is the generalized displacement vector of the coupled system, and $\{P\}$ is the generalized load vector of coupled system.

To induce the vibration of the structure, the train load input to the track–subgrade subsystem was in the form of the wheel–rail force. Subsequently, the time history analysis of the dynamic response process was carried out.

To highlight the sensitive factors and satisfy the accuracy of the analysis, the following assumptions were proposed to simplify the calculation model:

1) The horizontal and vertical boundaries of the model were expanded 10–15 times the span of the soil hole to minimize boundary effects.
2) The soil hole was generalized as an ellipsoidal soil hole located directly under the subgrade.
3) The analysis did not consider the horizontal force, reinforcement of the track structure, rail joints, and other details.
4) The rock and soil were considered as isotropic and homogeneous elastic–plastic materials.

The main body of the model included a CRTSII slab ballastless track structure, high-speed train, layered subgrade, soil hole, and foundation. Meanwhile, the train load was directly simulated along the track. Owing to the limited research time, the current research model was simplified, in which only a train with two carriages was simulated. In the future, a more comprehensive train–track–subgrade model that is more similar to the actual situation will be established for a more in-depth research.

The high-speed train has three parts: the wheelset, carriage, and bogie. The train, two bogies, and four wheelsets were connected by a suspension system. The following assumptions were made in this study:

1) The wheel set, carriage, and bogie were treated as rigid bodies, and eccentric action was not considered.
2) The connector element was adopted for the suspension system and did not consider nonlinear characteristics.
3) Only the vibration field generated by two carriages in a train was simulated, and the interaction between multiple carriages was not considered.
4) The train moved at a uniform speed along the track, and only the vertical force was considered [28].

The wheel was modeled with a practical size, and a wear-type tread was adopted for the wheel tread. The parameters of each part of the train were set by referring to the CRH3 type train. The track slab structure was modeled according to the CRTSII track, including the rail, fastener, track slab, cement–asphalt (CA) mortar, and bearing layer. Meanwhile, the solid parts were bound by a TIE connection. The rail

geometry of the model was simulated according to a standard section of a 60-kg rail.

The wheel–rail contact setting primarily considered the wheel–rail normal force (2) and wheel–rail tangential force (3):

$$P(t) = \left[\frac{1}{G} \Delta Z(t) \right]^{\frac{3}{2}}, \quad (2)$$

where G is the wheel–rail contact constant (m/N$^{2/3}$), which is equal to $3.86R^{-0.0115} \times 10^{-8}$ (m/N$^{2/3}$), in which R is the wheel radius (m), and $\Delta Z(t)$ is the elastic compression of the wheel/rail (m) at time is t;

$$F = \mu \times P(t) = \left[\mu_k + (\mu_s - \mu_k) e^{-d_c \gamma_{eq}} \right] \times P(t), \quad (3)$$

where μ_k is the dynamic friction coefficient, μ_s is the static friction coefficient, d_c is the attenuation coefficient, γ_{eq} is the relative sliding speed between the wheel and rail, and $P(t)$ is the wheel–rail normal force. The friction coefficient of the tangential behavior was set as 0.3. The damping material was set to light damping, and the mass damping coefficient α and stiffness damping coefficient β were needed to be input in the calculation process. The calculation formula is

$$C = \alpha M + \beta K, \quad (4)$$

where C is the spring stiffnesses, M is the mass, and K is the damping coefficient.

In the dynamic analysis, the constraint displacement on the model boundary produces vibration wave reflection, which did not conform to the characteristics of the vibration wave propagation to infinity, thereby affecting the accuracy of the results. In this study, a viscoelastic boundary was set at the bottom and around the model to simulate an infinite foundation, and the upper subgrade surface was not constrained. The normal and tangential damper coefficients and spring stiffness are given as

$$K_{BN} = \alpha_N \frac{G}{R}, \quad C_{BN} = \rho c_p; \quad (5)$$

$$K_{BT} = \alpha_T \frac{G}{R}, \quad C_{BT} = \rho c_s, \quad (6)$$

where K_{BN} and K_{BT} are the normal and tangential damping coefficients, respectively; C_{BN} and C_{BT} are the normal and tangential spring stiffnesses, respectively; R is the length of the artificial boundary; the tangential direction α_T is 2; normal direction $\alpha_T = 4$; G and ρ are the shear modulus and density of the soil, respectively; and c_p and c_s represent the longitudinal wave velocity and shear wave velocity, respectively. Thus, (6) was imported into ABAQUS.

The subgrade was modeled according to the standard size: a subgrade surface width of 8.6 m, surface layer thickness of 0.4 m, bottom layer thickness of 2.3 m, embankment filling thickness of 1.3 m, slope gradient of 1:1.5, foundation width of 50 m, and height of 30 m. The height was divided into the foundation soil layer and soluble bedrock. To eliminate the boundary effect, the model assumed a length of 100 m along

the train direction. The soil hole was located at 50 m. The grid density increased at the soil hole in the middle part directly below the subgrade. Considering the lower mechanical properties of the filled hole than that of the soil hole without filling, a hole with no filling was used. The soil hole was longitudinally located in the middle of the foundation model, and vertically located in the contact between the sedimentary soil and soluble rock layers. The soil hole had an ellipsoidal shape with a span of 2.5 m and height of 1.25 m. To improve the calculation efficiency and accuracy of the model, the mesh density was increased at the soil hole and subgrade. The rail and track structures were set as an elastic model, and the rock and soil in the subgrade and foundation were modeled using the Mohr–Coulomb ideal elastic–plastic material constitutive model. The model expressed the stability of the subgrade and possible collapse under different loads. The results of the subgrade and foundation grid division are shown in Fig. 1, and the final model is shown in Fig. 2.
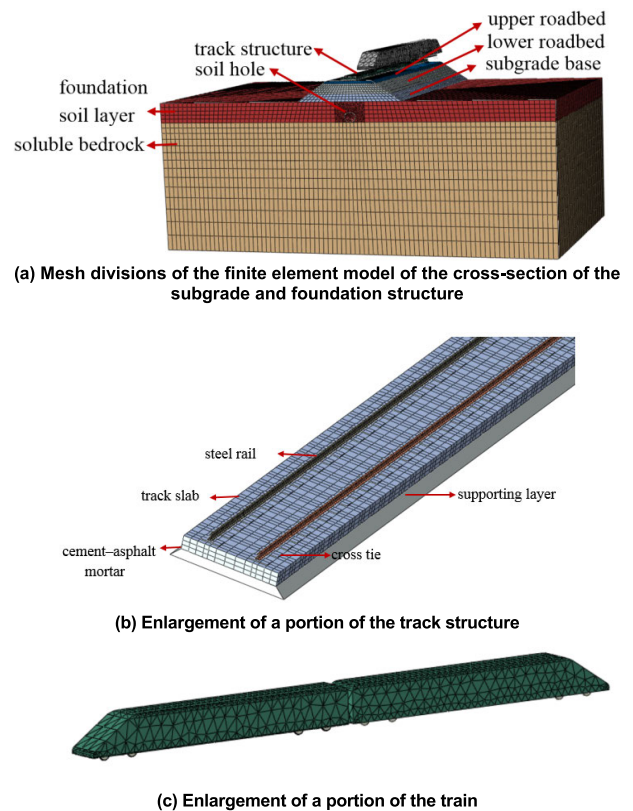

(a) Mesh divisions of the finite element model of the cross-section of the subgrade and foundation structure

(b) Enlargement of a portion of the track structure

(c) Enlargement of a portion of the train

FIGURE 1. Mesh generation of the model.

According to the geological conditions, the foundation was composed of limestone and clay. Based on existing literature, the physical, mechanical, and subgrade damping parameters used in the model are listed in Table 1 and 2.

2) RATIONALITY VERIFICATION OF THE KARST COLLAPSE SIMULATION

To verify the accuracy of the simulation results of the soil hole karst collapse, the calculation results of the

TABLE 1. Modeling parameters of different track structures.

Structure	Parameter	Unit	Value	Parameter	Unit	Value
Rail	Elastic modulus	GPa	210	α	s^{-1}	0.0328
	Poisson's ratio		0.3	β	s^{-1}	0.0031
	Section area	cm^3	76.45			
	Density	kg/m^3	7800			
Track slab	Elastic modulus	GPa	35.5	α	s^{-1}	0.0983
	Poisson's ratio		0.2	β	s^{-1}	0.0092
	Length × width × Thickness	m×m×m	100×2.55×0.2			
	Density	kg/m^3	2500			
CA mortar	Elastic modulus	MPa	7000	α	s^{-1}	0.0983
	Poisson's ratio		0.2	β	s^{-1}	0.0092
	Thickness	M	0.03			
	Density	kg/m^3	1800			
Supporting layer	Elastic modulus	GPa	22	α	s^{-1}	0.0983
	Poisson's ratio		0.2	β	s^{-1}	0.0092
	Span × thickness	m×m	(2.95/3.25)×0.3			
	Density	kg/m^3	2500			
Fastener	Vertical stiffness	N/m	$4.5×10^7$	Lateral damping	N·s/m	$3.625×10^4$
	Lateral stiffness	N/m	$3.0×10^2$	Longitudinal damping	kN/group	9
	Vertical damping	N·s/m	$6.0×10^4$	Spacing	m	0.6

TABLE 2. Subgrade modeling parameters.

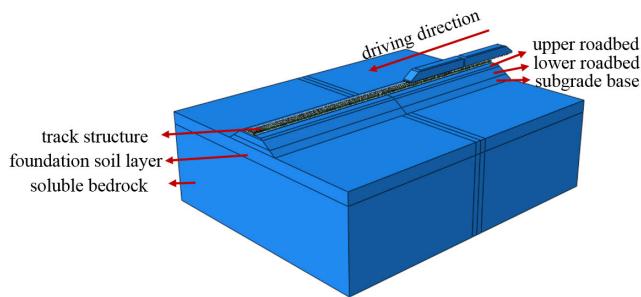| Type	Elastic modulus (MPa)	Poisson's ratio	Density (g/cm^3)	Cohesion (KPa)	Internal friction angle (deg)	α (s^{-1})	β (s^{-1})
Surface of the roadbed	220	0.25	21	35	43.0	0.2620	0.0244
Bottom of the roadbed	130	0.30	1900	13	28.0	0.2293	0.0214
Subgrade	50	0.20	1800	30	25.0	0.2750	0.0305
Limestone	190	0.25	26.5	20	44.3	0.2454	0.0016
Clay	16	0.25	18.5	32	25.0	0.2454	0.0016

FIGURE 2. Schematic of the environmental dynamic analysis model.

model were compared with the theoretical analysis results. In existing transportation engineering research, cylindrical and funnel-shaped soil hole collapse types are mainly considered. In this study, the cylindrical collapse evolution model was taken as an example for the comparative calculation. He *et al.* [29] deduced a formula for the critical collapse height of a cylindrical soil hole using the limit equilibrium theory

$$H_0 = \frac{\left(4\alpha\beta c + R\gamma - 2\alpha^2\beta q - 2c\right)}{2\gamma\alpha^2\beta}$$
$$+ \frac{\sqrt{\left(2\alpha^2\beta q - 4\alpha\beta c + 2c - R\gamma\right)^2 + 4\alpha^2\beta qR\gamma}}{2\gamma\alpha^2\beta}$$

(7)

where H_0 is the critical height (m), R is the radius of the soil hole (m), γ is the unit weight of the soil layer, c is the soil cohesion (kPa), φ is the internal friction angle of the soil mass, q is the overlying load (kPa), $\alpha = \tan(45° - \varphi/2)$, and $\beta = \tan\varphi$. By applying the appropriate parameters, the critical collapse height H_0 of 2.3 m was obtained. During the verification calculation, a stable load of 700 KPa was applied on the top of the model. As the theoretical formula does not include elliptical soil holes, the shape of the soil hole was simplified to a circle with a radius of 1 m.

The model simulated the upward development of the soil hole into seven stages. With the development of the soil hole, the thickness of the overburden was 26, 22, 18, 14, 10, 6, and 2 m, respectively. The settlement deformation of the foundation surface at different stages of the soil hole development is shown in Fig. 3(a). The stability of the foundation can be evaluated using the inclined deformation i [30], which refers to the ratio of the vertical and lateral displacement of the ground surface. When $i \leqslant 3$ mm/m, the foundation is considered stable. When $3 < i \leqslant 6$ mm/m, the foundation is considered to be basically stable. When $i \geqslant 6$ mm/m, the foundation is deemed unstable. Thus, the surface tilt deformation value is obtained, as shown in Fig. 3(b) and Table 3.

Through the simulation of the underlying soil hole, the stability analysis and calculation show that the soil hole instability led to subgrade collapse when the thickness of the
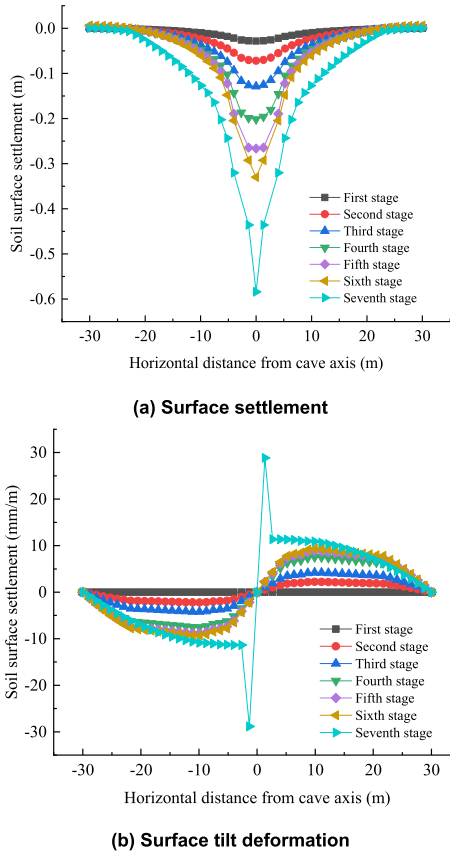
(a) Surface settlement

(b) Surface tilt deformation

FIGURE 3. Surface settlement and inclined deformation during the upward soil hole development.

TABLE 3. Stability of the upward development of the soil hole.

Stage	Overburden thickness (H/m)	Maximum settlement (ω/mm)	Maximum tilt deformation (i_{max})	Stability
1	26.00	28.16	0.053	stable
2	22.00	71.84	2.212	stable
3	18.00	128.89	4.203	basically stable
4	14.00	201.49	7.521	unstable
5	10.00	266.38	8.848	unstable
6	6.00	300.01	9.335	unstable
7	2.00	584.09	28.847	collapse

overlying soil layer is approximately 2 m, which is similar to the theoretically calculated critical collapse height of 2.3 m. Therefore, the simulation result of the model for soil hole karst collapse is verified.

B. VIBRATION MONITORING AND ANALYSIS

Train vibrations have nonlinear characteristics; thus, it is not sufficient to study them only by theory and calculations, and field monitoring is still the most direct and effective method of monitoring. In this study, a typical section of the Guizhou section of the Shanghai–Kunming high-speed railway was selected for the vibration monitoring of the surrounding

environment of the subgrade when a train with eight carriages passed through. The amplitude frequency and attenuation law of the vibration load under traffic conditions were examined.

1) SURVEY OF THE FIELD VIBRATION MONITORING

CRH2 high-speed train was the main vehicle type investigated in the test section. The monitoring subgrade section height was 3 m. The 891-2 vibration picker, developed by the China Seismological Bureau (Fig. 4), was selected. It has an acceleration resolution of 1×10^{-5} m/s^2 and maximum range of 40 m/s^2. A 16-channel data acquisition instrument and DASP software were used for the data acquisition with a maximum sampling rate of 256 kHz/channel (Fig. 5). A flow chart of the on-site vibration monitoring is shown in Fig. 6.

FIGURE 4. Model 891-2 vibration picker.
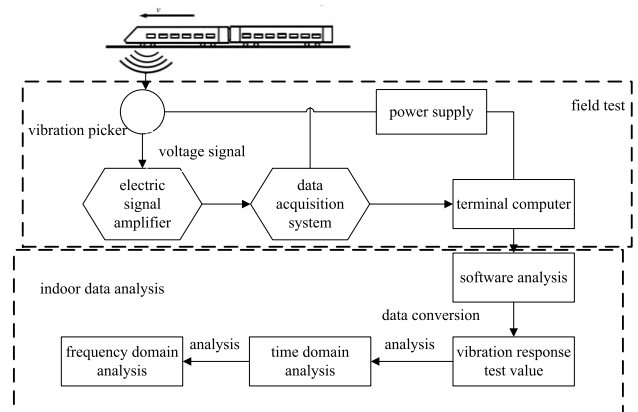

FIGURE 5. Data acquisition instrument.

FIGURE 6. Flow chart of the field vibration monitoring.

2) SITE MONITORING PLAN

The selection of the monitoring section directly affects the accuracy of the monitoring results. The monitoring

section was primarily selected based on its position in the straight-line section to reduce the interference of the additional load when the train runs in the curved section. In addition, the monitoring site was flat and open, which provided a good field of vision, ensuring that the equipment could monitor the entire train vibration process before the high-speed train arrived at the section. The monitoring location position was also established to be as close to the railway line as possible to maximize the monitoring data. The distance between the monitoring points was 3.0 m. The vertical vibrations were simultaneously monitored. The layout of the monitoring points is shown in Fig. 7.
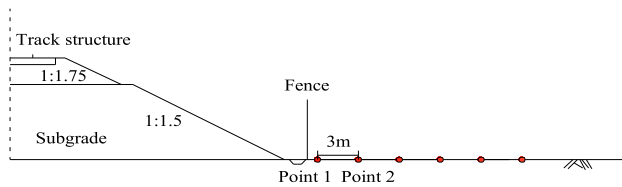
FIGURE 7. Schematic of the monitoring points.

3) TIME DOMAIN ANALYSIS OF THE VIBRATION MONITORING RESULTS

In this study, the field data collection and subsequent analysis of the vertical vibration during train passes were carried out. Fig. 8 shows the monitoring results of the time history response to the vertical vibration acceleration when the train passed at 229 km/h. The vertical vibration acceleration amplitudes of the different measuring points are summarized in Fig. 9.

As a full-length train with eight carriages passed through, vibration was continuously observed for 6.3 s. Moreover, the vibration acceleration time history curve of each measuring point exhibited no evident differences apart from the amplitude. When the wheelset passed through the section, the amplitude of the acceleration time history curve fluctuated significantly. The maximum values of the vibration acceleration of measuring points no. 1–6 were 0.153, 0.099, 0.075, 0.054, 0.040, and 0.029 m/s^2, respectively. The ground vibration intensity showed nonlinear attenuation with an increase in the distance between the measuring points and subgrade. The maximum value was 5.28 times that of the minimum value, and the total attenuation rate was 81.05%. The vibration acceleration was attenuated by 54.55%, and the attenuation and deceleration rate at points 2–6 decreased. This indicates that when the soil hole along the railway is far from the subgrade structure, the stability of the subgrade will not be greatly affected.m/s^2.

4) FREQUENCY DOMAIN ANALYSIS OF THE VIBRATION MONITORING RESULTS

The power spectrum of the vibration monitoring signal was obtained through FTT between the time and frequency domains, and the power spectrum of each measuring point was compared. The relationship between the time history signal $X(t)$, power spectrum $G(\omega)$, and correlation function $R(\tau)$ of the vibration wave is shown in Fig. 10.

The time domain signal $X(t)$ can be resolved into a frequency function by FTT:

$$X(\omega) = \int_{-\infty}^{+\infty} x(t)e^{-j\omega t}dt, \tag{8}$$

where ω denotes a continuous frequency variable. A difference exists in the distribution of energy generated by the vibration at each frequency, which can be described by the self-power spectrum and calculation formula:

$$G(\omega) = X(\omega) \cdot X^*(\omega). \tag{9}$$

The vibration acceleration time history signal was normalized by FTT using MATLAB. The vibration acceleration spectra of the different measuring points were obtained, as shown in Fig. 11.

Increased high-frequency vibrations and wider frequency range were observed at the measuring points closer to the subgrade. The dominant vibration frequencies at measuring points 1–6 were 10–60, 10–50, 10–30, 0–20, 0–10, and 0–10 Hz, respectively. The dominant vibration frequency decreased from 10–60 Hz at measuring point 1 to 0–10 Hz at measuring point 6, in which the vibration of 20–60 Hz almost dissipated. This indicates that the increase in the propagation distance of the vibration wave increased the attenuation speed of the high-frequency vibration, whereas that of the low-frequency vibration decreased, resulting in the peak value of the spectrum curve becoming closer to the low-frequency vibration.

5) DYNAMIC RESPONSE VALIDATION OF THE MODEL

To verify the accuracy of the model, the generalized model built according to the site conditions was compared with the field-measured data. A comparison between the time history curve of the simulated and monitored vibration wave is shown in Fig. 12.

The model was used to simulate the vibration response of a pair of carriages passing through the section. Owing to the limitations of the research time and computing equipment in this study, a calculation time of 2 s was selected to reduce the computing time and workload. The longitudinal length of the numerical model was 100 m, and the on-site track length was regarded to have infinite extension, which affected the propagation of the vibration waves. Moreover, this caused the prolonged vibration of a single train carriage during the numerical simulation, compared to that obtained during the on-site monitoring. The vibration acceleration amplitudes of measuring points 1–4 calculated by the model were 0.168, 0.116, 0.095, and 0.075 m/s^2, respectively, whereas the field monitoring results were 0.153, 0.099, 0.075, and 0.054 m/s^2, respectively, with the errors of 9.00%, 17.17%, 26.67%, and 38.89%, respectively. These errors are attributed to the
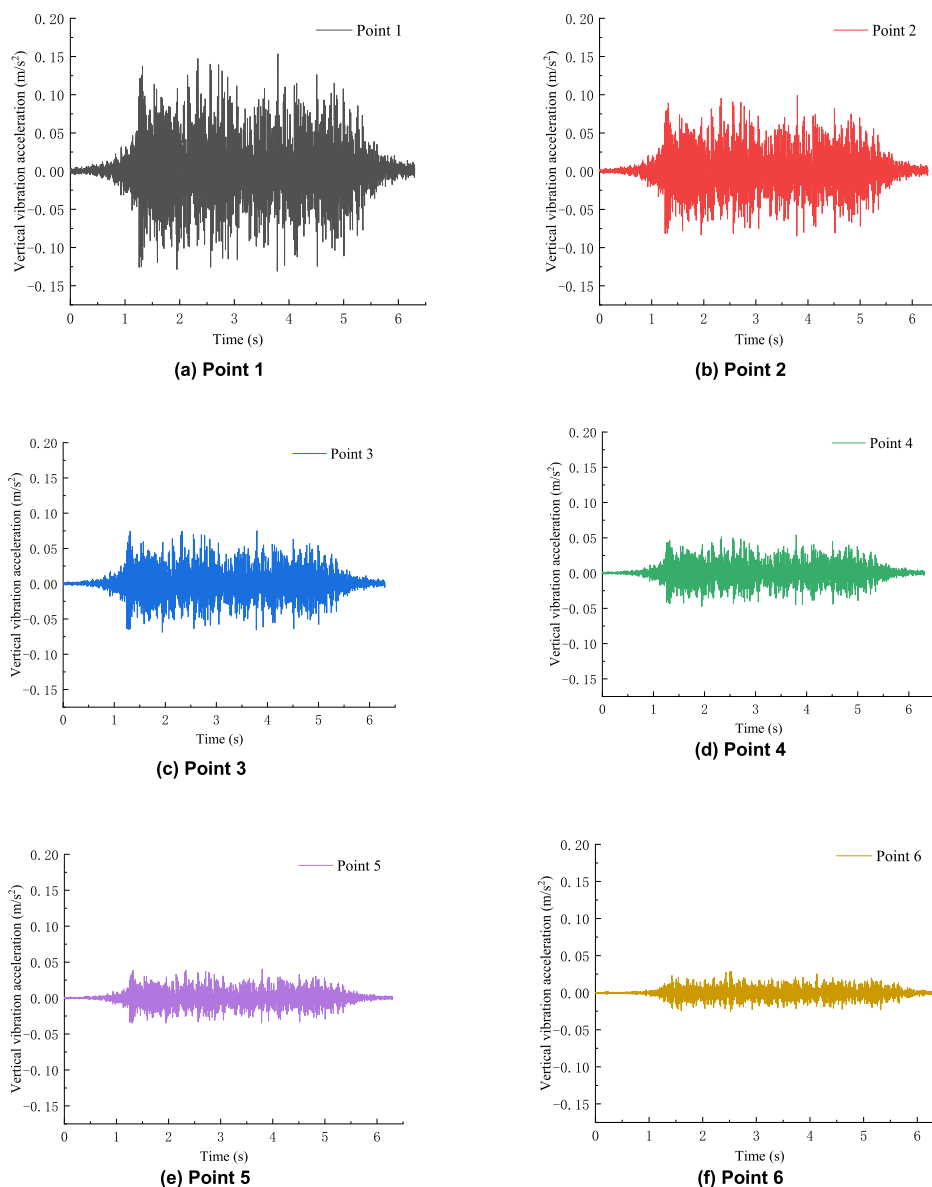
FIGURE 8. Time history curve of the vibration acceleration at different measuring points during train passes.

attenuation of the vibration waves by the on-site plants and structures, indicating that the measured values were lower than the simulated values. Further, as the measuring point was farther from the subgrade, the error increased. The different results is also attributed to the non-uniform on-site damping, which was regarded as a fixed value during the modelling. In addition, the on-site railway line can be regarded as infinite extension and the transmission of the train vibration has gradually increasing time-varying characteristics as the train moves away from the subgrade. However, the model only simulated a track length of 100 m, and the train vibration was directly loaded, which caused the longer vibration duration of a single carriage for the simulated value than that of the monitoring value. Moreover, higher vibration amplitude was observed in the first 0.5 s.

The two data groups of measuring point 1, which have the smallest measured and simulated amplitude errors, and highest curve fit, were analyzed by one-way ANOVA with a significance level α of 0.05. The mean and variance of the measured data were 0.0011 and 0.0015, respectively, whereas that of the simulated data were 0.0009 and 0.0031, respectively. The significance value p of the two groups of data was $0.071 > \alpha$, indicating there is no significant difference between the two groups of data and accuracy of the model in measuring point 1. In addition, the vibration propagation farther from the subgrade has minimal impact on the stability of the soil hole and subgrade. The measuring points close to the subgrade have small error values. Therefore, this model can be applied to the dynamic response analysis of soil within the subgrade.
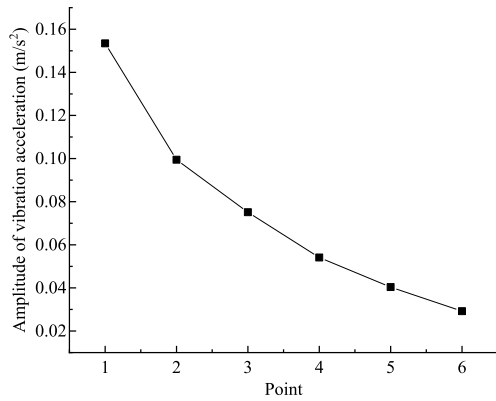
FIGURE 9. Amplitude curve of the vibration acceleration at different measuring points.
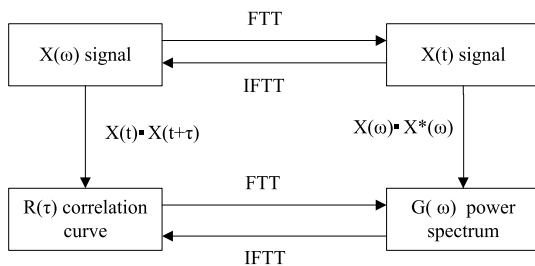

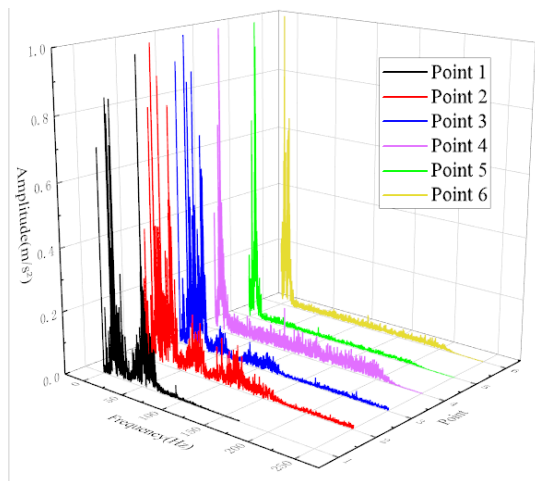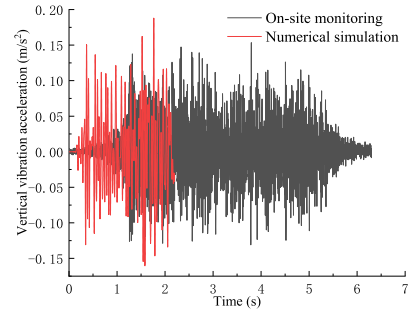**FIGURE 10.** Schematic of the conversion between the time and frequency domains.
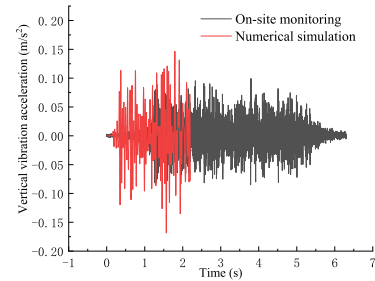

FIGURE 11. Spectra of the vibration acceleration at different measuring points.

(a) Point 1

(b) Point 2

(c) Point 3

(d) Point 4

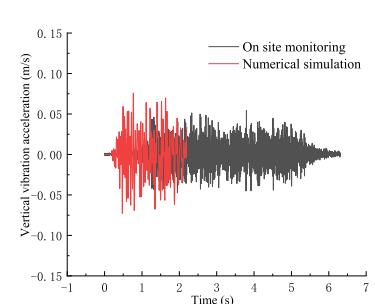**FIGURE 12.** Comparison of time history curves of the vibration waves.

IV. RESULTS AND DISCUSSION

The curve characteristics of the dynamic parameters under different conditions quantitatively express the influence of soil holes, different axle loads, and different vehicle operating speeds on roadbed stability. Consequently, the change trend along the depth of the influence can be summarized. The high-speed railway subgrade stability transformation in karst

areas under different working conditions is quantitatively evaluated.

A. DISTRIBUTION CHARACTERISTICS OF THE SUBGRADE DYNAMIC DISPLACEMENT

In this section, the dynamic displacement in the vertical direction is studied by selecting a train axle load of 16 t, driving speed of 250 km/h, subgrade filling height of 4 m,

and buried soil tunnel depth of 2 m. The time history curves of the vertical dynamic displacements at different structural layers of the subgrade centerline when the train passes over the subgrade with underlying soil tunnel and that without soil tunnel are shown in Figure 13.
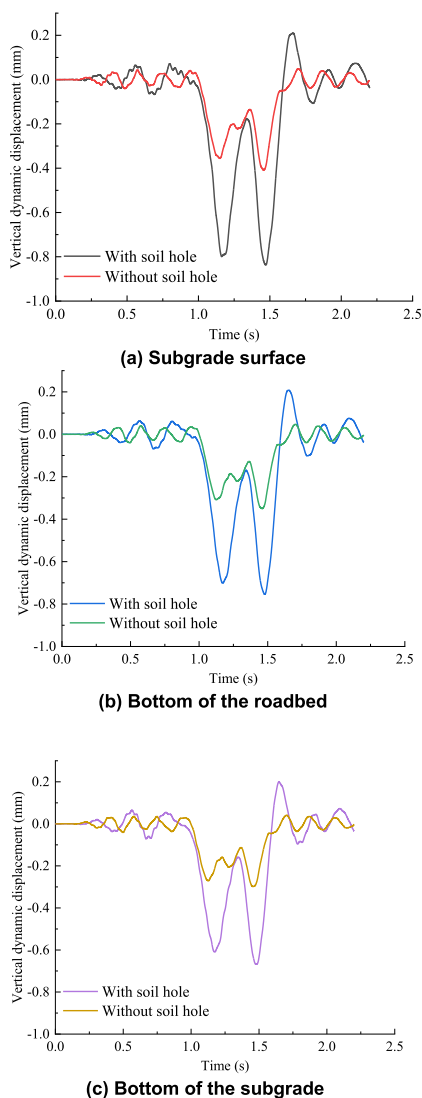
the vertical dynamic displacement of different layers and the stability of the subgrade. Under the same working conditions, the vertical dynamic displacement distribution along the transverse direction of the subgrade when the train passed over the soil hole in the middle section of the subgrade is shown in Fig. 14.
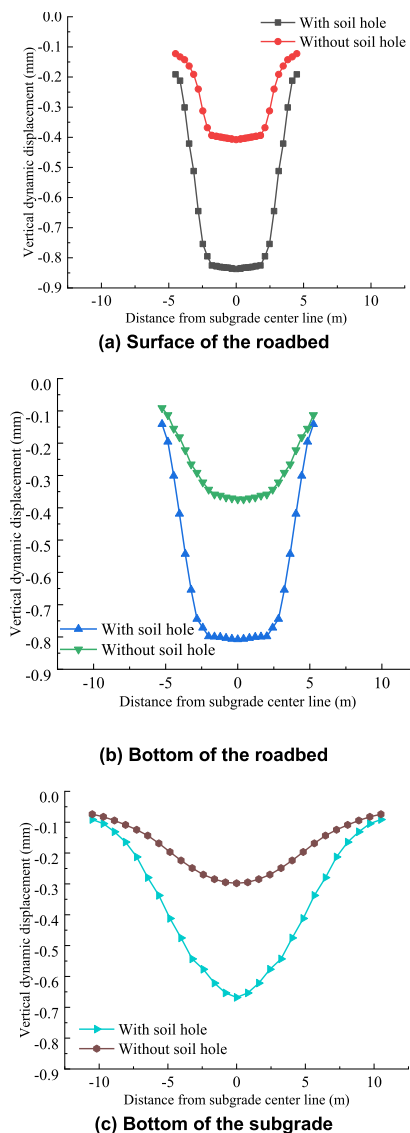

FIGURE 13. Time history curve of the dynamic displacement of different structural layers of the high-speed railway subgrade in a karst area.

FIGURE 14. Transverse distribution characteristics of the dynamic displacements of the different structural layers of the high-speed railway subgrade in karst area.

When the train passed directly above the soil hole, the maximum vertical dynamic displacement was observed on the subgrade surface. The maximum vertical dynamic displacement was 0.408 and 0.837 (105.15% increase) mm, when there was no soil hole and where there was an underlying soil hole, respectively. Comparing the different layers, the maximum vertical dynamic displacement of the bottom layer and bottom of the subgrade were 0.351 and 0.298 mm, respectively, when there was no soil hole, whereas those with the underlying soil hole were 0.754 and 0.668 mm, respectively (increase of 114.81% and 124.16%, respectively). With increasing depth, the soil cavity had increasing influence on

The vertical displacements of the different subgrade layers were symmetrically distributed along the middle line of the subgrade. In addition. the settlement under the supporting layer of the track slab was clearly larger than that on both sides. Further, the dynamic displacement exhibited a U shape and had small changes in the range of the supporting layer. With an increase in the depth, the vertical dynamic displacement gradually attenuated, and the influence of the track structure on the shape of the vertical displacement curve
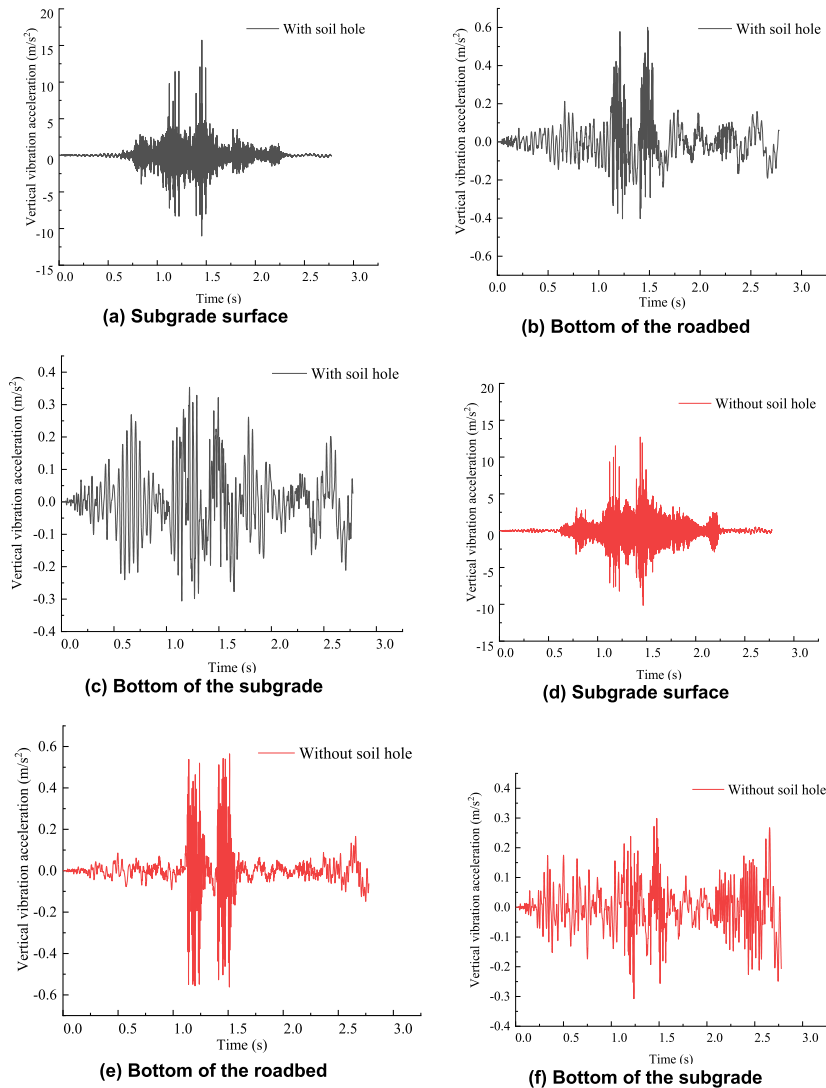
FIGURE 15. Time history curve of the vertical vibration acceleration of the different structural layers of the high-speed railway subgrade in a karst area.

further decreased, gradually changing from a U-shaped distribution to a V-shaped distribution. Moreover, the vertical dynamic displacement of each structure layer was always greater when there is no soil hole.

B. DISTRIBUTION CHARACTERISTICS OF THE SUBGRADE VIBRATION ACCELERATION

Under the same working conditions, the vertical vibration acceleration generated by the train under operating conditions was observed to be greater than that in the transverse and longitudinal directions. Thus, this section presents the analysis of the calculation results of the vertical vibration acceleration time history curve of the different layers in the middle line of the subgrade when the train was passing through the subgrade section, as shown in Fig. 15.

When the first bogie passed directly above the subgrade soil hole, the first peak acceleration appeared, and the

vibration attenuation occurred after the bogie passed through. During the attenuation process, the second bogie passed through, and the acceleration again exhibited a peak value with a superposition effect. After the train passed through completely, the acceleration gradually returned to its initial state. With an increase in the subgrade depth, the instantaneous peak effect of the vibration acceleration caused by a bogie passing through the surface layer gradually decreased, and the curve changed from a concentrated bimodal shape to a spindle shape. This is because the wheel–rail vibration observed when the bogie passed through was considerably higher than that at other times, thereby forming a peak. However, with an increase in depth, the energy distribution gradually became uniform during propagation. The energy concentration in the subgrade surface layer gradually decreased with an increase in depth. After reaching a certain depth of the subgrade structural layer, the distribution of the

vibration energy became more uniform than that in the surface layer, the peak effect disappeared, and the curve amplitude became more uniform. The maximum vertical vibration acceleration appeared on the subgrade surface. The maximum vertical vibration acceleration of the subgrade with and without a soil hole were 12.72 and 15.71 m/s², respectively. The maximum vertical vibration acceleration increased by 23.51% when there was a soil hole. In contrast, when there was no soil hole, the maximum vertical vibration acceleration of the bottom layer and bottom of the subgrade were 0.56 and 0.31 m/s², respectively, whereas those with an underlying soil hole were 0.60 and 0.35 m/s² respectively (increase of 7.14% and 12.90%, respectively). Thus, the soil holes loosened the surrounding soil structure, and the subgrade without soil holes was denser. The vibration response was evident when the soil holes lie in the same position [33], [34].

C. DISTRIBUTION CHARACTERISTICS OF THE DYNAMIC STRESS OF SUBGRADE

Under the same working conditions, the vertical dynamic stress time history curves of the different layers in the subgrade centerline are shown in Fig. 16.

The underlying soil hole had no significant influence on the vertical dynamic stress time history curve of each structural layer of the subgrade. In addition, the vertical dynamic stress response decreased with increasing depth. The maximum vertical dynamic stress of the subgrade with and without the soil hole was 7.19 and 9.43 kPa, respectively. When there was no soil hole, the maximum vertical dynamic stress of the bottom of the roadbed and subgrade bottom were 3.90 and 2.98 kPa, respectively, whereas those with an underlying soil hole were 3.96 and 2.82 kPa, respectively. Under the same working conditions, the vertical dynamic stress distribution along the transverse direction of the subgrade when the train passed above the soil hole in the middle section of the subgrade is shown in Fig. 17.

The vertical dynamic stress was symmetrically distributed along the middle line of the subgrade. The distribution of the dynamic stress on the top and bottom of the subgrade bed presents a "W" shape, which first slightly increased in the range of the bearing layer, and then sharply increased at the edge of the bearing layer. This was attributed to the stress concentration at the edge of the bearing layer, while there was no direct train dynamic stress input outside the bearing layer. Subsequently, the dynamic stress dropped sharply until it approached zero. With an increase in depth, the dynamic stress distribution on the subgrade surface was relatively slow, and the amplitude was considerably less than that on the surface and bottom of the subgrade bed. The center of the subgrade had the largest dynamic stress. With the increase in the distance from the center of the subgrade, the dynamic stress gradually decreased to zero.

The distribution of the vertical dynamic displacement, dynamic acceleration, and dynamic stress along the depth direction with and without the soil hole is shown in Fig. 18. The amplitudes of the vertical dynamic displacement,
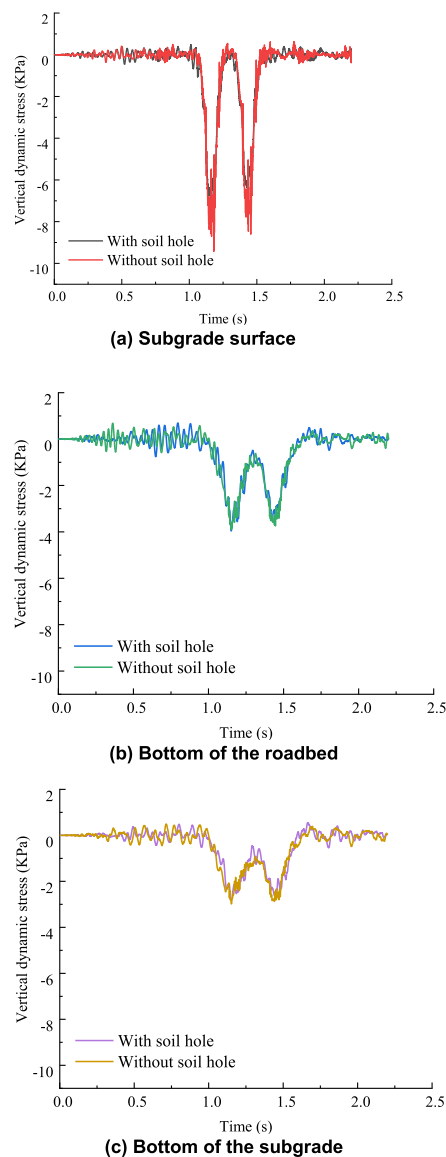

FIGURE 16. Time history curve of the dynamic stress of the different structural layers of the high-speed railway subgrade in a karst area.

vibration acceleration, and vertical dynamic stress decreased nonlinearly with an increase in depth. In addition, at each depth, the vertical dynamic displacement was greater without the soil hole.

When there was no soil hole, the vertical dynamic displacement in the bottom of the roadbed, bottom layer of the subgrade, and foundation were attenuated by 6.15%, 13.97%, and 37.96%, respectively, compared with the surface layer of the foundation. In contrast, with an underlying soil hole, the attenuations were 8.62%, 10.43%, and 22.45%, respectively. The attenuation area was primarily in the foundation, which was evident when there was no soil hole. With an underlying soil hole, the vibration acceleration rebounded near the soil hole owing to the reflection of the vibration wave from the bottom of the hole. Moreover, the acceleration difference is
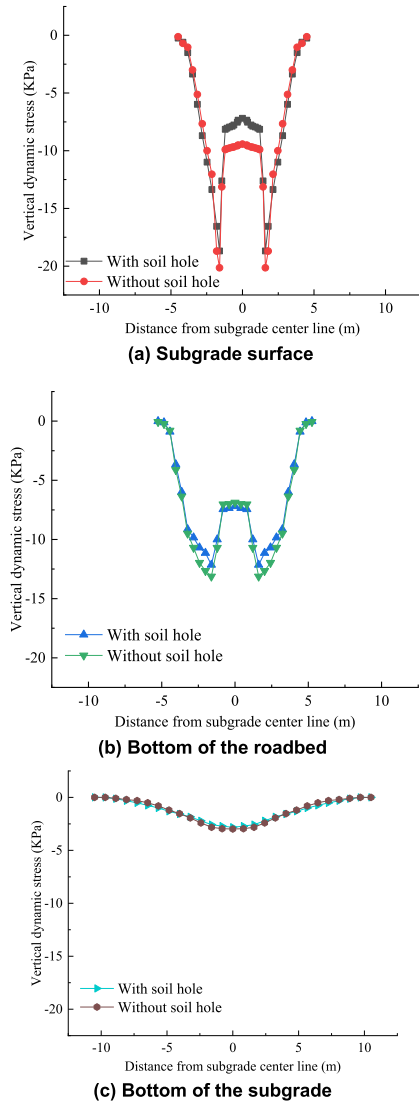
FIGURE 17. Transverse distribution characteristics of the dynamic stress in different structural layers of the high-speed railway subgrade in the karst area.

FIGURE 18. Amplitude of the dynamic parameters at different depths of the high-speed railway subgrade in a karst area.

higher closer to the soil hole. The acceleration attenuation without a soil hole was approximately 45.34%, 24.92%, and 11.53% in the bottom of the roadbed, bottom layer of the subgrade, and foundation, respectively. With an underlying soil hole, the acceleration attenuation was approximately 47.56%, 21.55%, and −3.46%, respectively. The attenuation area was primarily in the bottom layer of the subgrade, and the acceleration attenuation was evident when there was no soil hole.

The amplitude of the vertical dynamic stress decreased nonlinearly with an increase in depth without a soil hole, the dynamic stress decreased by approximately 43.35%, 18.80%, and 27.14% at the bottom of the subgrade bed, bottom of the subgrade, and foundation, respectively. With an underlying soil hole, the dynamic stress decreased by approximately 39%, 23%, and 27%, respectively, with the
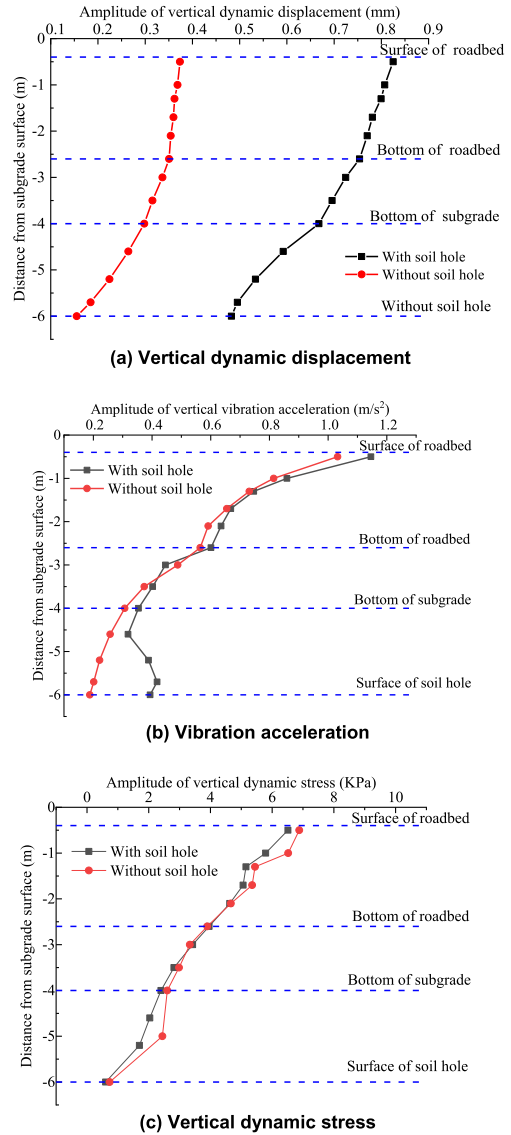
attenuation area of the dynamic stress primarily located at the bottom of the subgrade bed.

The dynamic characteristics of the high-speed railway subgrade in karst areas vary under different driving conditions and environments. Therefore, the difference in the underlying soil hole was subject to driving conditions was studied, along with the dynamic characteristics and stability of the subgrade under the condition of one-way traffic and different train axle loads and speeds.

D. INFLUENCE OF THE TRAIN AXLE LOAD ON DYNAMIC RESPONSE

This section presents the dynamic response of the subgrade under different axle loads of 10, 12, 14, 16, 18, 20, and 22 t with a driving speed of 250 km/h, embankment filling height
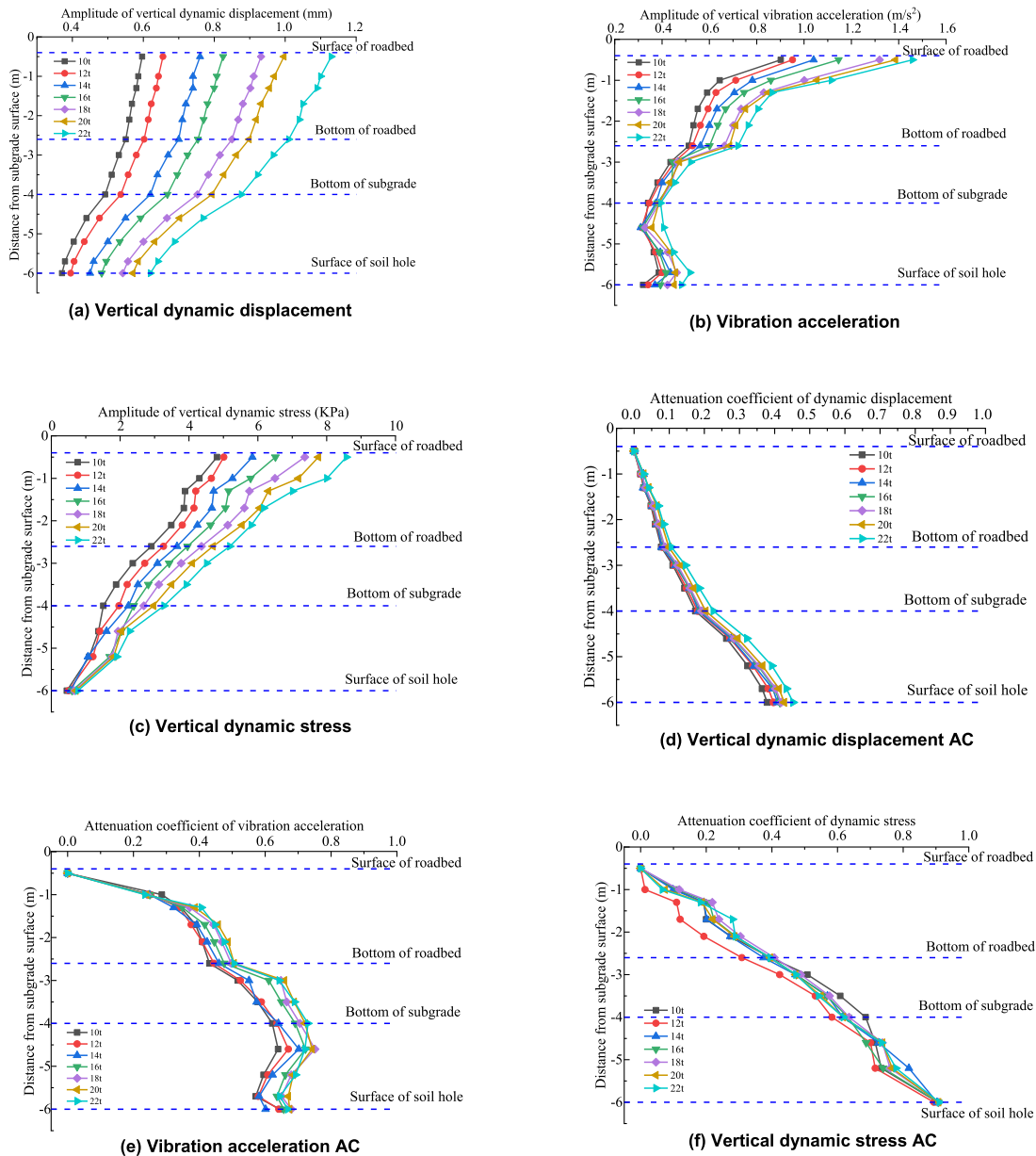
FIGURE 19. Amplitude of dynamic parameters and its AC change curve with depth in different axle load.

of 4 m, and soil hole buried depth of 2 m. Fig. 19 shows the distribution characteristics along the depth direction of the maximum amplitude of the vertical dynamic displacement, dynamic acceleration, and dynamic stress curves at the center of the subgrade under different axle loads and the corresponding attenuation coefficient (AC).

With the increase in depth, the difference of the vertical dynamic displacement of the axle load from 10 t to 22 t gradually decreased from 0.51 mm of the surface layer of the subgrade bed to 0.25 mm of the top of the soil hole, which decreased by 50.98%. In addition, the difference in the acceleration decreased by 71.43% from 0.56 to 0.16 m/s². The difference of the vertical dynamic stress decreased by

91.49% from 3.76 to 0.32 kPa. When the train axle load increased from 10 t to 22 t, the amplitude of the vertical dynamic displacement decreased by 37.87%, 39.68%, 40.79%, 41.50%, 41.83%, 42.74%, and 45.24%, respectively, from the surface layer of the roadbed to the top of the soil hole. The corresponding amplitude of the vertical vibration acceleration decreased by 64.49%, 64.13%, 60.11%, 65.65%, 67.95%, 67.42%, and 66.87%, and that of the vertical dynamic stress decreased by 90.61%, 37%, 90.32%, 90.71%, 90.91%, 90.80%, and 91.02%, respectively. This shows that the dynamic effect of the train axle load on the subgrade decreased with an increase in depth. Moreover, when the axle load increased, the dynamic response

parameter amplitude increased, which affected the stability of the subgrade.

The uneven settlement of the subgrade surface is the main factor for driving safety. Thus, the dynamic response characteristics of the subgrade surface under different axle loads were studied (dynamic acceleration of 10, 16, and 22 t). The time history curves of the vertical dynamic displacement, dynamic acceleration, and dynamic stress of the subgrade surface are shown in Fig. 20.

As the axle load of the train increased from 10 t to 22 t, the amplitude of vertical dynamic displacement on the subgrade surface increased from 0.60 to 1.15 mm (increase of 91.67%) and the amplitude of the vibration acceleration increased from 9.88 to 19.74 m/s^2 (increase of 99.80%). The amplitude of the vertical dynamic stress increased from 4.80 to 9.99 kPa (increase of 108.13%). As the train axle load increased, the vertical dynamic displacement and dynamic stress amplitude of the subgrade surface linearly increased with a relatively constant rate of increase. The amplitude of the vibration acceleration increased nonlinearly, and the rate of increase was faster when the train axle load was less than 18 t, and relatively slow when the train axle load was greater than 18 t. Thus, increasing the train axle load had a significant influence on the dynamic response and stability of the subgrade.

E. INFLUENCE OF THE TRAIN SPEED ON THE DYNAMIC RESPONSE

With the increase in train speed, the wheel–rail effect was strengthened, and the dynamic response of the environmental vibration field to the subgrade structure and the underlying soil hole considerably changed. In this section, the axle load of the train was 16 t, the embankment filling height was 4 m, the buried depth of the soil hole was 2 m, and the vehicle speeds were 160, 180, 200, 250, 300, 350, and 400 km/h. The deformation characteristics and dynamic response of the subgrade surface under different driving speeds were analyzed. Fig. 21 shows the distribution characteristics and AC of the maximum amplitude of the vertical dynamic displacement, dynamic acceleration, and dynamic stress curves at the center of the subgrade along the depth direction under seven axle loads.

As the train speed increased, the vertical dynamic displacement and dynamic stress amplitude of each structure layer and soil hole position in the same subgrade depth increased, while showing an almost linear decay along the depth direction. The acceleration did not always increase with the increase in the vehicle speed and decayed nonlinearly along the depth direction. With the increase of the depth, the dynamic displacement difference of the surface layer of the subgrade bed and top of the soil hole was 0.48 and 0.45 mm, respectively, which is almost negligible. The influence of the speed on the dynamic displacement did not weaken with the increase of the depth and the difference in vertical vibration acceleration increased from 0.16 to 0.40 m/s^2 (increase of 150%). The influence of the

(a) Vertical dynamic displacement

(b) Vertical dynamic stress

(c) 10 t vibration acceleration

(d) 16 t vibration acceleration

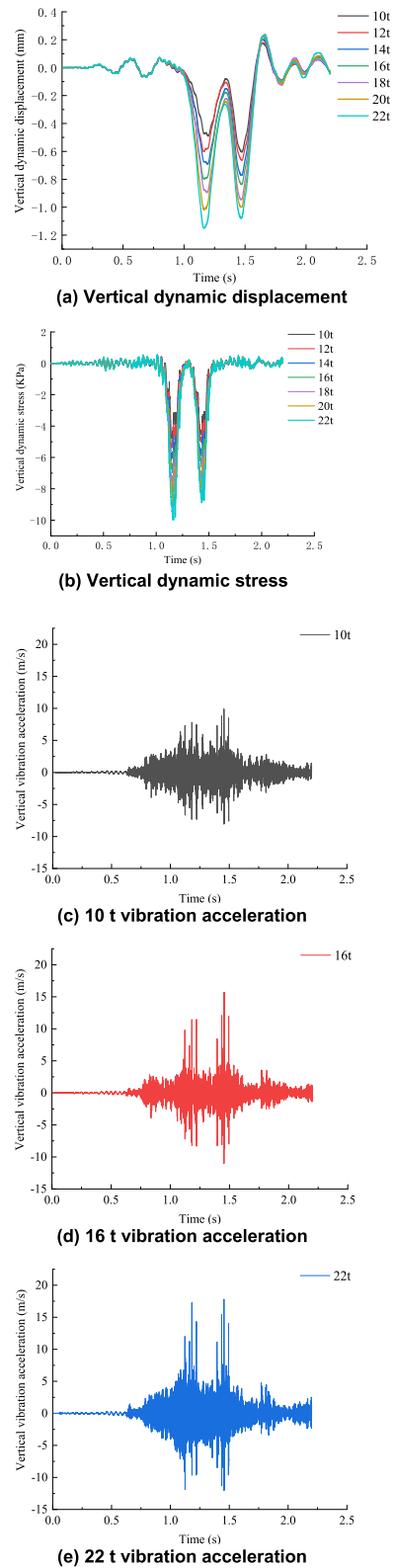(e) 22 t vibration acceleration

FIGURE 20. Time history curve of subgrade surface dynamic parameters in different axle load.

running speed on the vibration acceleration increased with the depth, and the difference in vertical dynamic stress decreased from 1.78 kPa in the surface layer of the subgrade bed to
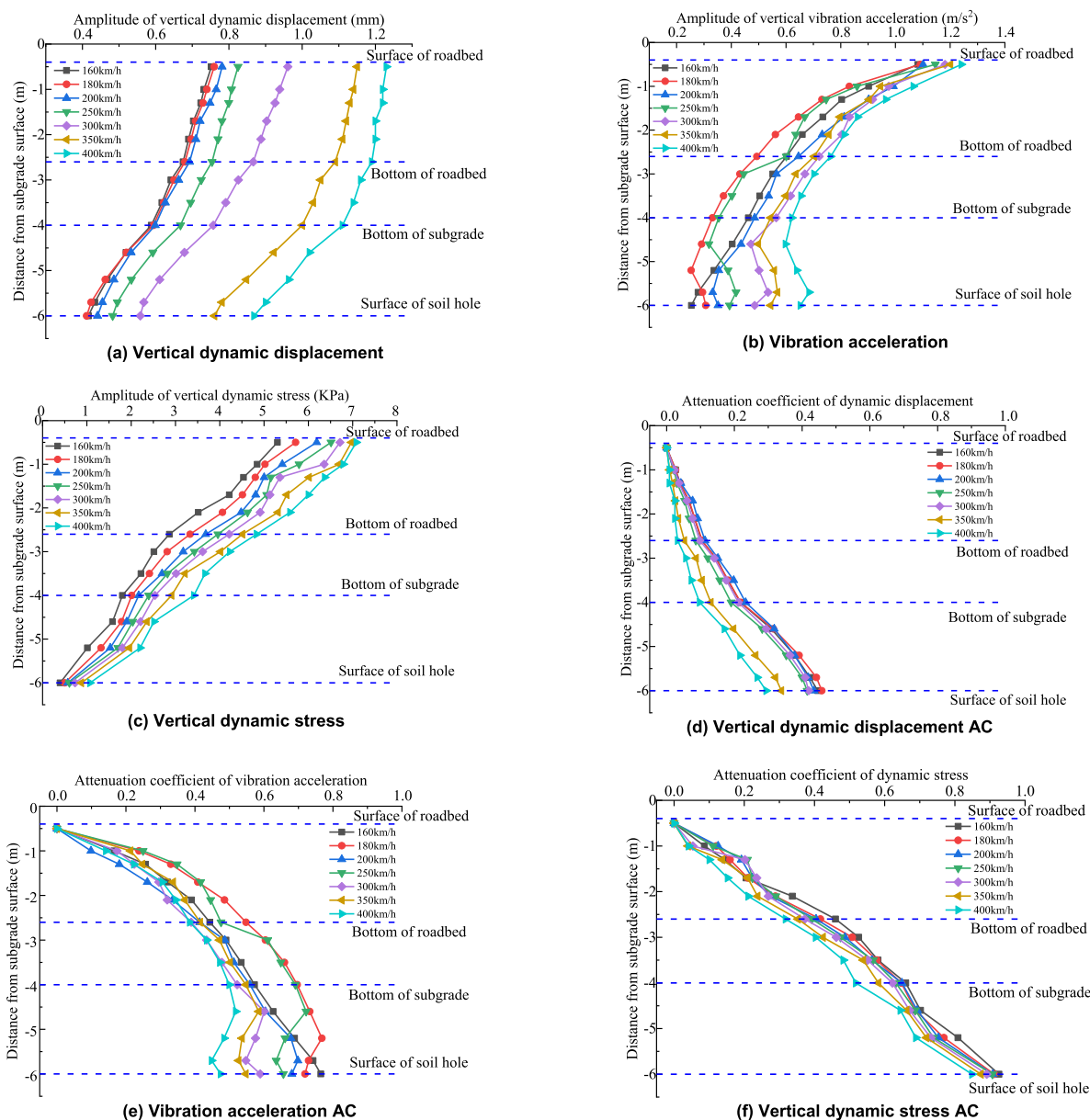
FIGURE 21. Amplitude of the dynamic parameters and its AC change curve with depth under different train speed.

0.67 kPa at the top of the soil hole (decrease of 62.36%). This shows that the influence of the train running speed on the dynamic stress gradually weakens with an increase in depth. When the train speed was 160, 180, 200, 250, 300, 350, and 400 km/h, the vertical dynamic displacement amplitude decreased by 44.62%, 45.82%, 43.50%, 41.50%, 41.92%, 33.87%, and 29.37%, respectively, from the surface layer of subgrade bed to the top of the soil hole. This indicates that the vertical dynamic displacement attenuation along the depth decreased when the train speed was greater than 300 km/h. The acceleration amplitude decreased by 76.50%, 71.91%, 68.10%, 65.65%, 58.92%, 54.74%, and 47.44%, respectively from the surface of the subgrade bed

to the top of the soil hole, which indicates that the attenuation of the vibration acceleration along the depth weakened with the increase of the train running speed. Meanwhile, the amplitude of the vertical dynamic stress decreased by 92.54%, 91.22%, 90.80%, 90.71%, 89.10%, 87.43%, and 84.89%, at the train speed of 160, 180, 200, 250, 300, 350, and 400 km/h, respectively. The dynamic stress attenuation along the depth was more apparent; however, with the increase in train speed, the dynamic stress attenuation along the depth decreased.

The time history curves of the vertical dynamic displacement, dynamic acceleration, and dynamic stress on the subgrade surface when the representative train running speeds
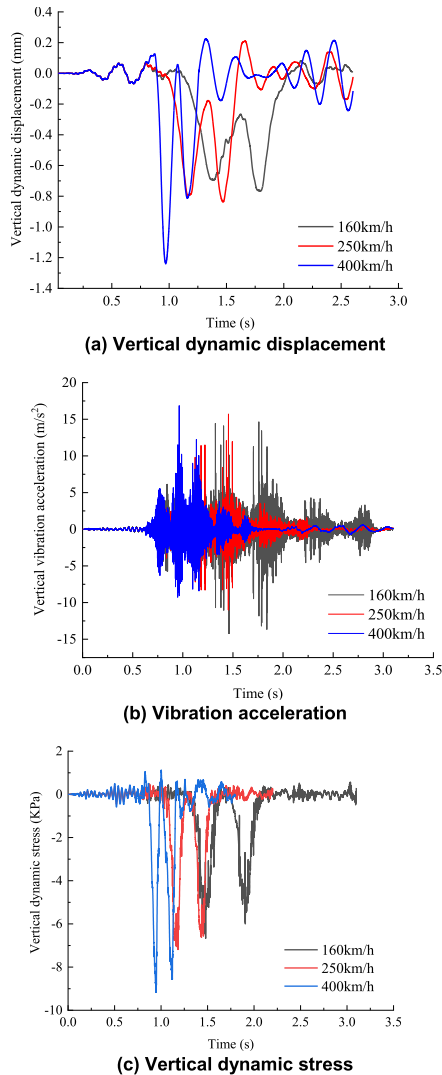
(a) Vertical dynamic displacement

(b) Vibration acceleration

(c) Vertical dynamic stress

FIGURE 22. Time history curve of the subgrade surface dynamic parameters at different speeds.

were 160, 250, and 400 km/h are shown in Fig. 22. The figure shows that the time of the vertical dynamic displacement, dynamic acceleration, and peak dynamic stress was delayed at different speeds. On the surface of the subgrade, the amplitude of the vertical dynamic displacement increased from 0.76 to 1.24 mm (increase of 63.16%) as the train speed increased from 160 to 400 km/h. Meanwhile, the amplitude of the dynamic acceleration increased from 14.65 to 16.84 m/s^2 (increase of 14.95%), whereas the amplitude of the vertical dynamic stress increased from 6.66 to 9.16 kPa (increase of 37.54%). With the increase in train speed, the dynamic displacement amplitude of the subgrade surface increased nonlinearly. The rate of increase was lower when the speed was less than 250 km/h, whereas significant increase was noted when the speed was greater than 250 km/h. The amplitude of the vibration acceleration did not increase with the increase in vehicle speed due to the acceleration of the load moving speed and decreased loading

time on the subgrade. The dynamic stress amplitude increased nonlinearly with a the lower rate of increase when the speed was less than 250 km/h and significant increase when the speed was greater than 250 km/h. Therefore, the train speed had a significant influence on the stability of the subgrade, vertical dynamic displacement, dynamic stress, and dynamic acceleration.

V. CONCLUSION

In this study, the time-frequency characteristics and attenuation law of the vibration acceleration caused by train vibrations at different measuring points in karst areas were studied by monitoring and finite element analysis. The study area was the Guizhou section of the Shanghai–Kunming high-speed railway. A dynamic analysis model of the soil mass of the train–track–subgrade was established, and the dynamic response of the subgrade to the train vibration loads under different conditions was studied. The primary conclusions drawn are as follows:

1) The dominant frequency of the high-speed train surrounding environment vibration was concentrated in the range of 10–60 Hz. With the increase in the propagation distance, the attenuation was faster for high-frequency vibration and slower for low-frequency vibration, resulting in the peak value closer to low-frequency vibration in the spectra.

2) Under the train operation conditions, the vertical deformation and vibration acceleration of the soil hole under the subgrade was larger, and the deformation and dynamic characteristics were more pronounced. The soil hole had a significant impact on the stability of the subgrade and safety of the train operation.

3) The dynamic displacement, vibration acceleration, and dynamic stress of the subgrade structure and soil hole increased with an increase in the train axle load, significantly affecting the stability of the soil hole and subgrade structure.

4) There were apparent differences observed on the dynamic displacement, acceleration, and dynamic stress of the subgrade structure and soil hole position under different train speeds. The faster train speed resulted in the more apparent dynamic response, thereby a significant impact on the stability of the soil hole and subgrade.

REFERENCES

[1] X. F. Cao and H. L. Li, "Typical zone division of Karst development in China," *Adv. Geosci.*, vol. 8, no. 4, pp. 845–851, 2018, doi: 10.12677/AG.2018.84092.

[2] B. An, L. Gao, T. Xin, G. Xiang, and J. Wang, "A novel approach of identifying railway track rail's modal frequency from wheel-rail excitation and its application in high-speed railway monitoring," *IEEE Access*, vol. 7, pp. 180986–180997, Dec. 2019, doi: 10.1109/ACCESS.2019.2959444.

[3] S. Ma, L. Gao, X. Liu, and J. Lin, "Deep learning for track quality evaluation of high-speed railway based on vehicle-body vibration prediction," *IEEE Access*, vol. 7, pp. 185099–185107, Dec. 2019, doi: 10.1109/ACCESS.2019.2960537.

[4] J. Guo, H. Shi, R. Luo, and P. Wu, "Parametric analysis of the car body suspended equipment for railway vehicles vibration reduction," *IEEE Access*, vol. 7, pp. 88116–88125, May 2019, doi: 10.1109/ACCESS.2019.2918777.

[5] H. Bai, D. Ma, and Z. Chen, "Mechanical behavior of groundwater seepage in Karst collapse pillars," *Eng. Geol.*, vol. 164, pp. 101–106, Sep. 2013, doi: 10.1016/j.enggeo.2013.07.003.

[6] B. Vigna, A. Fiorucci, C. Banzato, P. Forti, and J. D. Waele, "Hypogene gypsum Karst and sinkhole formation at Moncalvo (Asti, Italy)," *Zeitschrift für Geomorphol.*, vol. 54, no. 2, pp. 285–306, Mar. 2010, doi: 10.1127/0372-8854/2010/0054S2-0015.

[7] L. Pando, J. A. Pulgar, and M. Gutiérrez-Claverol, "A case of man-induced ground subsidence and building settlement related to Karstified gypsum (Oviedo, NW Spain)," *Environ. Earth Sci.*, vol. 68, no. 2, pp. 507–519, Jan. 2013, doi: 10.1007/s12665-012-1755-3.

[8] G. Kaufmann and D. Romanov, "Structure and evolution of collapse sinkholes: Combined interpretation from physico-chemical modelling and geophysical field work," *J. Hydrol.*, vol. 540, pp. 688–698, Sep. 2016, doi: 10.1016/j.jhydrol.2016.06.050.

[9] W. G. Xu and G. R. Zhao, "On mechanism of Karst collapse," *J. China Coal Soc.*, vol. 2, pp. 3–13, Jun. 1986, doi: CNKI:SUN:MTXB.0.1986-02-000.

[10] M. Heidari, G. R. Khanlari, A. R. T. Beydokhti, and A. A. Momeni, "The formation of cover collapse sinkholes in north of Hamedan, Iran," *Geomorphology*, vol. 132, nos. 3–4, pp. 76–86, Sep. 2011, doi: 10.1016/j.geomorph.2011.04.025.

[11] H. Xiao, H. Li, and Y. Tang, "Assessing the effects of rainfall, groundwater downward leakage, and groundwater head differences on the development of cover-collapse and cover-suffosion sinkholes in central Florida (USA)," *Sci. Total Environ.*, vol. 644, pp. 274–286, Dec. 2018, doi: 10.1016/j.scitotenv.2018.06.273.

[12] X. F. Shi, "Study on the roof stability of concealed Karst cave under pile foundation loading in Karst areas," Ph.D. dissertation, Wuhan Inst. Rock Soil Mech., Chin. Acad. Sci., Wuhan, China, 2005.

[13] Y. J. Zhang, W. G. Cao, M. H. Zhao, and H. Zhao, "Interval fuzzy judgment method for roadbed stability in Karst area," *Chin. J. Geotech. Eng.*, vol. 33, pp. 38–44, Jan. 2011, doi: 10.3724/SP.J.1077.2011.00271.

[14] E. Yan, J. Cheng, and L. Liu, "Stability analysis and evaluation of soil cave foundation under the role of groundwater in Karst area," *Int. J. Intell. Syst. Appl.*, vol. 1, no. 1, pp. 60–67, Oct. 2009, doi: 10.5815/ijisa.2009.01.07.

[15] C. Jiang, M.-H. Zhao, and W.-G. Cao, "Stability analysis of subgrade cave roofs in Karst region," *J. Central South Univ. Technol.*, vol. 15, no. S2, pp. 38–44, Apr. 2010, doi: 10.1007/s11771-008-0433-9.

[16] R. L. Michalowski, "Stability charts for uniform slopes," *J. Geotech. Geoenviron. Eng.*, vol. 128, no. 4, pp. 351–355, Apr. 2002, doi: 10.1061/(ASCE)1090-0241(2002)128:4(351).

[17] E. M. Dawson, W. H. Roth, and A. Drescher, "Slope stability analysis by strength reduction," *Géotechnique*, vol. 49, no. 6, pp. 835–840, Dec. 1999, doi: 10.1680/geot.1999.49.6.835.

[18] Y. S. Ye, "Dynamic response performance of high speed railway subgrade," *Railway Eng.*, vol. 10, pp. 7–12, Oct. 2015, doi: 10.3969/j.issn.1003-1995.2015.10.02.

[19] H. Takemiya and X. Bian, "Substructure simulation of inhomogeneous track and layered ground dynamic interaction under train passage," *J. Eng. Mech.*, vol. 131, no. 7, pp. 699–711, Jul. 2005, doi: 10.1061/(ASCE)0733-9399(2005)131:7(699).

[20] G. Lefeuve-Mesgouez and A. Mesgouez, "Ground vibration due to a high-speed moving harmonic rectangular load on a poroviscoelastic half-space," *Int. J. Solids Struct.*, vol. 45, nos. 11–12, pp. 3353–3374, Jun. 2008, doi: 10.1016/j.ijsolstr.2008.01.026.

[21] Y. Q. Cai, L. Guo, R. J. Jardine, Z. X. Yang, and J. Wang, "Stress–strain response of soft clay to traffic loading," *Géotechnique*, vol. 67, no. 5, pp. 446–451, May 2017, doi: 10.1680/jgeot.15.P.224.

[22] P. Galvín and J. Domínguez, "Experimental and numerical analyses of vibrations induced by high-speed trains on the Córdoba–Málaga line," *Soil Dyn. Earthq. Eng.*, vol. 29, no. 4, pp. 641–657, Apr. 2009, doi: 10.1016/j.soildyn.2008.07.001.

[23] P. Salvador, J. Real, C. Zamorano, and A. Villanueva, "A procedure for the evaluation of vibrations induced by the passing of a train and its application to real railway traffic," *Math. Comput. Model.*, vol. 53, nos. 1–2, pp. 42–54, Jan. 2011, doi: 10.1016/j.mcm.2010.07.016.

[24] X.-Z. Ling, S.-J. Chen, Z.-Y. Zhu, F. Zhang, L.-N. Wang, and Z.-Y. Zou, "Field monitoring on the train-induced vibration response of track structure in the Beiluhe permafrost region along Qinghai–Tibet railway in China," *Cold Regions Sci. Technol.*, vol. 60, no. 1, pp. 75–83, Jan. 2010, doi: 10.1016/j.coldregions.2009.08.005.

[25] X. Ling, F. Zhang, Z. Zhu, L. Ding, and Q. Hu, "Field experiment of subgrade vibration induced by passing train in a seasonally frozen region of Daqing," *Earthq. Eng. Eng. Vib.*, vol. 8, no. 1, pp. 149–157, Mar. 2009, doi: 10.1007/s11803-009-8090-z.

[26] Y. Qiu, M. Fang, X. Zhang, and Y. Wei, "Dynamic analysis of structural adaptivity of ballastless track substructure of high-speed railway," *J. Southwest Jiaotong Univ.*, vol. 46, pp. 183–188, Apr. 2011, doi: 10.3969/j.issn.0258-2724.2011.02.001.

[27] X. L. Song and W. M. Zhai, "Dynamic stress distribution of the infrastructure of CRTS II slab ballastless track under high speed moving load," *China Railw. Sci.*, vol. 33, no. 4, pp. 1–7, Jul. 2012, doi: 10.3969/j.issn.1001-4632.2012.04.01.

[28] S. Yang, K. Song, and G. Zhu, "Stochastic process and simulation of traction load for high speed railways," *IEEE Access*, vol. 7, pp. 76049–76060, Jun. 2019, doi: 10.1109/ACCESS.2019.2921093.

[29] Z. He, Y. Yang, X. Zeng, and S. Liu, "Response analysis of subgrade deformation in evolution of concealed soil cave," *J. Central South Univ. Sci. Technol.*, vol. 49, no. 12, pp. 3068–3076, Dec. 2018, doi: 10.11817/j.issn.1672-7207.2018.12.021.

[30] Y. G. He, S. Xiong, and S. C. Wu, "Studies on indicators for tolerable displacement and deformation of expressway above mined-out area," *Mining Metall. Eng.*, vol. 33, no. 12, pp. 27–30, Jun. 2019, doi: 10.3969/j.issn.0253-6099.2013.02.007.

[31] F. X. Wang, "Numerical simulation and vibrational characteristic analysis of high-speed railway due to environmental vibrations based on ABAQUS," M.S. thesis, School Civil Eng., Beijing Jiaotong Univ., Beijing, China, 2014.

[32] H. Wu, P. Wu, K. Xu, J. Li, and F. Li, "Research on vibration characteristics and stress analysis of gearbox housing in high-speed trains," *IEEE Access*, vol. 7, pp. 102508–102518, Jul. 2019, doi: 10.1109/ACCESS.2019.2931424.

LI XIN received the B.Sc. and M.Sc. degrees from the School of Highway Engineering, Chang'an University, Xi'an, China, in 2013 and 2015, respectively. He is currently pursuing the Ph.D. degree with the School of Civil and Architectural Engineering, Beijing Jiaotong University, Beijing, China. His research interests include highway and railway subgrade engineering, traffic geological engineering environment, traffic geological disaster prevention, and subgrade and pavement material engineering.

BAI MINGZHOU received the Ph.D. degree in engineering from Chengdu University of Technology, in 2000. He did his postdoctoral research at Beijing Jiaotong University, from 2000 to 2002. He is currently a Professor and a Doctoral Supervisor with the School of Civil and Architectural Engineering, Beijing Jiaotong University. His research interests include subgrade and pavement engineering, traffic geological environment, rail transit, and road transportation.

WEI ZIJUN received the bachelor's degree in railway engineering from the School of Geotechnical Engineering, Shijiazhuang Tiedao University, in June 2018, and the master's degree in road and railway engineering from the School of Civil and Architectural Engineering, Beijing Jiaotong University, in June 2021.

He currently works as an Assistant Engineer with China Railway Fourth Survey and Design Institute Group Company Ltd., engaged in engineering economic research.

SHI HAI received the Ph.D. degree from the School of Civil and Architectural Engineering, Beijing Jiaotong University, in July 2017. He graduated from the Postdoctoral Station of Civil Engineering, Department of Water Resources and Hydropower Engineering, Tsinghua University, in May 2018. He is currently working with the School of Civil and Architectural Engineering, Beijing Jiaotong University, engaged in research on subgrade engineering, traffic geological environment, and traffic infrastructure operation and maintenance. His main research interests include subgrade disease detection and treatment, ground collapse, and line engineering geological disaster prevention and control.

LI PENGXIANG received the bachelor's degree in hydraulic engineering from the School of Water Resources, North China University of Water Resources and Electric Power, in 2017, and the master's degree in transportation engineering from the School of Civil and Architectural Engineering, Beijing Jiaotong University, in 2019, where he is currently pursuing the Ph.D. degree in road and railway engineering with the School of Civil and Architectural Engineering. He is engaged in research on karst disaster prevention and control.

ZHANG YE received the bachelor's degree in road and bridge engineering from the School of Transportation, Wuhan University of Technology, in 2019. He is currently pursuing the master's degree in road and railway with the School of Civil and Architectural Engineering, Beijing Jiaotong University. His research interests include subgrade and pavement engineering and traffic geological environment.

● ● ●